Barrier-free Interface Electron Transfer on PtFe-Fe_2C Janus–like Nanoparticles Boosts Oxygen Catalysis

ABSTRACT: Precise tunings desired of size, shape, composition, structure, and surface strain of PtM-based nanocrystals was were well demonstrated in further improving the ORR catalytic performance.8-27 These demonstrations excellent reports are more related to precise surface tuning of PtM nanocrystals for achieving the optimized oxygen binding energy and thus the enhanced ORR catalytic activity.

Designing the interface catalyst with the strong interfacial synergistic effect between two different kinds of materials has rarely been demonstrated for ORR in acid solution. Here we report a new class of the interface catalyst: PtFe-Fe_2C Janus-like NPs. PtFe-Fe_2C Janus-like NPs show higher catalytic activity for the oxygen reduction than either PtFe or Fe_2C NPs in an acidic/alkaline electrolyte. The specific/mass activities of the PtFe-Fe_2C Janus-like NPs for oxygen reduction reaction are 11.8/7.1 times higher than commercial Pt/C catalyst in an acidic electrolyte, respectively. These NPs are also stable in the electrochemical acid conditions. Density functional theory simulations reveal that a barrier-free interface electron transfer on PtFe-Fe_2C Janus–like nanoparticles in enhancing oxygen reduction reaction activities. This prepared interface catalyst also displayed enhanced catalytic activity for hydrogen evolution reactions and electrochemical detection of H_2O_2 than either PtFe or Fe_2C NPs.

The Na-based dual-ion batteries (NDIBs), combining both the advantages of Na-ion batteries and dual-ion batteries, are attracting more attention due to their merits of abundant source, low cost and high energy density. However, the main challenges faced by NDIBs are their low

capacity and poor cycling. Herein, we report a new ion storage mechanism for high-performance NDIBs using amorphous ordered mesoporous carbon (AOMC) as cathode. Unlike the graphite carbon that can only accommodates the PF_6^- anions (typical DIB system), the AOMC herein can both accommodate Na^+ cation and PF_6^- anion due to its amorphous and mesoporous feature, which is conceptually new dual ion system for achieving a much higher capacity. *Ex-situ* X-ray photoelectron spectroscopy, X-ray diffraction and Raman studies reveal that the disordered carbon in the AOMC can be transformed to the partial graphitic stacking in short range, improving both capacity and cycling stability of NDIBs. As a consequence, the AOMC delivers a highly reversible storage capacity of 136 mAh g^{-1} for over 800 cycles at a very high current density of 2.0 A g^{-1}, much higher than all the reported NDIBs.

The development of highly efficient catalysts for oxygen reduction reaction (ORR) is the key for high-performance commercially viable fuel cell devices and metal−air batteries.[1-3] Among all the potential catalysts, platinum (Pt) represents the essential element for ORR specifically in acidic electrolytes. Superior to monometal Pt, Pt-based alloy nanoparticles (NPs) by alloying late transition metals (M, where M = Fe, Co, Ni, Cu, *etc.*) offer much enhanced ORR catalysis due to the downshift of d-band center of Pt caused by the well-known ligand effect, resulting in the weakened binding energy of Pt to oxygen immediate species.[4-7] Precise tunings of size, shape, composition, structure and surface strain of PtM-based nanocrystals were demonstrated in further improving the ORR catalytic performance.[8-27] These excellent reports are more related to surface tuning of PtM nanocrystals for achieving the optimized oxygen binding energy and thus the enhanced ORR catalytic activity. Compared with surface catalyst, the interface catalyst is attracting more attention recently because the strong interface synergistic effect between two different kinds of materials may provide another interesting way for tuning the oxygen binding energy and electron transfer, and further boosting ORR catalytic performance. However, designing the interface catalyst with strong

interfacial effect has rarely been demonstrated for ORR in acid solution because of the lack of effective method for making such interface materials.[28]

Transition-metal carbides (TMCs) have recently received intensive attention due to their many outstanding properties, including high electrical and thermal conductivity, high melting point, excellent mechanical strength and hardness, chemical stability as well as the resistance against corrosion. Moreover, because of their special metallic structures with small carbon atoms in the interstitial voids of the densely packed host lattice, TMCs are endowed with the interstitial alloy properties, and attracting considerable attention in the field of catalysis.[29-31] Creating new interface catalysts by integrating the PtM alloy nanoparticles with transition metal carbides may be an excellent system for studying the interface-driven catalysis enhancement, however, achieving such heterostructured catalysts is still a grand challenge. Herein we report an effective strategy for making a new class of Janus-like PtFe-Fe_2C NPs that have the brand new property of barrier-free interface electron transfer for boosting ORR catalysis. PtFe-Fe_2C Janus-like NPs exhibit much higher catalytic activity for ORR than either PtFe or Fe_2C NPs in an acidic/alkaline electrolyte. They deliver unprecedented ORR performance with the specific and mass activities of 3.53 mA cm^{-2} and 1.50 A mg^{-1}_{Pt} at 0.9 V *versus* reversible hydrogen electrode (RHE) in all the reported FePt-based catalysts, 11.8 and 7.1 times higher than those of the state-of-the-art Pt/C catalyst in an acidic electrolyte. The density functional theory (DFT) calculations reveal that the synergy between PtFe and Fe_2C components not only produces a rich electronegativity for promoting the charge transfer of ORR, but also reducing or annihilating the energetic barriers of each intermediating steps. The PtFe-Fe_2C Janus-like NPs show good cycling stability for ORR with negligible activity decay over the course of 5,000 cycles. Furthermore, barrier-free interface electron transfer property of PtFe-Fe_2C Janus-like NPs makes them exhibit much higher catalytic activity for hydrogen evolution reaction (HER) and electrochemical detection of H_2O_2 than either PtFe or Fe_2C NPs. The current density of PtFe-Fe_2C Janus-like NPs for HER at -0.07 V in 0.5 M H_2SO_4 is 28.2 mA/cm^2, 2.9 times higher than that of the

Pt/C (9.6 mA/cm^2). They also exhibit excellent electrocatalytic activity for the electrochemical reduction of H_2O_2 with a very low detection limit of 2 nM. The present work demonstrates the first example in creating interface nanocatalysts with the barrier-free interface electron transfer property can boost electrocatalysis.

RESULTS AND DISCUSSION

Synthesis and characterization of PtFe-Fe$_2$C Janus-like NPs. The synthetic procedure of PtFe-Fe_2C Janus-like NPs is illustrated in **Fig. 1a**. In the first step, monodisperse PtFe-Fe_3O_4 Janus-like NPs were synthesized through one-pot approach according to a modified procedure.[32] Then, PtFe-Fe_2C Janus-like NPs were obtained by carbonizing treatment of PtFe-Fe_3O_4 Janus-like NPs in octadecylamine (OAm) under a Ar blanket at 320 ^oC. Herein, OAm can serve as both the carbon and hydrogen sources *via* the dehydrogenation and C−C cleavage reactions under high temperatures. This plays an important role in converting iron oxides directly into carbides in a reducing and carbonizing atmosphere.

Fig. 1b shows the typical transmission electron microscopy (TEM) image of representative PtFe-Fe_3O_4 Janus-like NPs. It is found that each NP consists of a dark part and a light-colored part, revealing its Janus-like feature. The black dots are PtFe with an average diameter of 6 nm, and light-colored parts are Fe_3O_4 with an average diameter of 13 nm. The compositional ratio of Pt to Fe in black dot of Janus-like NPs is determined to be 46/54 by inductively coupled plasma atomic emission spectroscopy (ICP-AES). After carburizing treatment, there are negligible morphology changes of Janus-like NPs (**Fig. 1c**). But the diameter of the Fe_2C NPs was a little bit expanded to 14 nm. **Fig. 1d** shows high-resolution TEM (HRTEM) image of PtFe−Fe_2C Janus-like NPs. The distances between two adjacent lattice fringes are measured to be 0.211 and 0.214 nm, corresponding to (-101) plane spacing (0.213 nm) of hexagonal Fe_2C, and (111) plane spacing (0.22 nm) of face-centered cubic (*fcc*) PtFe, respectively. The HAADF elemental mappings of PtFe−Fe_2C

Janus-like NPs shows that Fe evenly distribute throughout the whole NPs, but the distribution of Pt is mainly located at the dark part of NPs (**Supplementary Fig. 3**). The crystal structure of PtFe−Fe_2C NPs was also characterized by X-ray diffraction (XRD). **Fig. 1e** shows the representative XRD patterns of 8 nm PtFe (**Supplementary Fig. 4**), 16 nm Fe_2C (**Supplementary Fig. 5**) and 6−14 nm PtFe−Fe_2C NPs. In the case of PtFe NPs, there are three peaks located at 40°, 46.7°, and 68.4°, being in consistent with the (111), (200) and (220) reflections of *fcc* PtFe (JCPDS Card No. 29-0717). The characteristic diffraction peaks of Fe_2C are observed at 37.7°, 41.5°, 43.2°, 57.3° and 68°, assigned to the (100), (002), (101), (102) and (110) reflections of hexagonal Fe_2C (JCPDS Card No. 36-1249). Two sets of peaks from the PtFe-Fe_2C NPs match well with those of the PtFe and Fe_2C NPs, respectively, further confirming that these Janus-like NPs are composed of PtFe and Fe_2C NPs.

The electronic structure of Pt and C in PtFe−Fe_2C NPs was further characterized by X-ray photoelectron spectroscopy (XPS). **Supplementary Fig. 6a** shows XPS of 8 nm PtFe NPs and 6-14 nm PtFe−Fe_2C Janus-like NPs. Compared with the 8 nm PtFe NPs, the 6-14 nm PtFe−Fe_2C NPs have a ~0.26 eV decrease in electron binding energy of Pt_{4f}. This change may modify the electrocatalytic activity of PtFe in the ORR process. The high-resolution C_{1s} spectra of PtFe−Fe_2C Janus-like NPs are shown in **Supplementary Fig. 6b**. The peaks at 284.8 eV, 286.4 eV and 288.3 eV are observed, attributable to the surface contaminated carbon, the organic N–C and O–C species. Notably, a strong low-binding energy peak signal at 283.1 eV is detected, representing the typical metallic Fe–C bonding, similar to the previously reported Ni_3C compounds.[36] These results further support the fact that the as-prepared Janus-like nanostructure consists of PtFe and Fe_2C NPs.

ORR performance. The ORR electrocatalytic performances of the Janus-like PtFe-Fe_2C, PtFe NPs, Fe_2C NPs and commercial Pt/C were tested in 0.1M $HClO_4$ solution. Before the electrochemical evaluation, the catalysts were prepared by loading the NPs on Vulcan XC-72 carbon support by sonication, and then treated with acetic acid to remove the surfactant around NPs. The carbon-supported catalysts were made as the homogeneous ink, and further deposited on glassy

carbon rotating disk electrode (GC-RDE). **Fig. 2a** shows the cyclic voltammograms (CVs) of different catalysts recorded at room temperature in N_2-sutated 0.1 M $HClO_4$ solution. On the basis of the charge associated with the hydrogen desorption charges, the electrochemically active surface area (ECSA) of PtFe-Fe_2C Janus-like NPs was determined to be 42.5 m^2/g, similar to that of PtFe NPs (41.1 m^2/g) and lower than that of commercial Pt/C (68.9 m^2/g). **Fig. 2b** shows the ORR polarization curves of different catalysts in O_2-saturated 0.1 M $HClO_4$ solution at a rotation rate of 1600 rpm. The ORR specific activity of the PtFe-Fe_2C Janus-like NPs reaches 3.53 mA/cm^2 at 0.9 V (*vs* reversible hydrogen electrode (RHE)), 2.7 and 11.8 times greater than those of the PtFe NPs and commercial Pt/C, respectively (**Fig. 2d**). The ORR mass activity of PtFe-Fe_2C Janus-like NPs is 1.50 mA/mg_{Pt}, 2.9 and 7.1 times higher than those of PtFe NPs and commercial Pt/C, respectively. These indicate that the PtFe-Fe_2C Janus-like NPs are much more active than PtFe NPs and commercial Pt/C, which is the best PtFe-based ORR electrocatalysts reported to date (**Supplementary Table 1**).

Durability is another important parameter to evaluate the performance of ORR catalysts. Accelerated durability tests (ADT) of the catalysts were conducted by cycling the potential between 0.6 and 1.1 V in an O_2-saturated 0.1 M $HClO_4$ at room temperature, close to the typical potential range at fuel cell cathode. After 5,000 cycles, there is almost no ORR polarization curve shift on PtFe-Fe_2C Janus-like NPs (**Fig. 2e**) whereas under the same condition, the commercial Pt/C shows a big degradation of 30 mV for half-wave potential (**Fig. 2f**). The structure of carbon-supported PtFe-Fe_2C Janus-like NPs after the durability test was characterized by TEM, showing that there was negligible morphology change of PtFe-Fe_2C Janus-like NPs after long-term cycles (**Supplementary Fig. 8**). Furthermore, ICP-AES results show very small Fe/Pt composition decrease from 70/30 to 67/33 after 5,000 potential cycles. The strong interface synergistic effect of PtFe-Fe_2C Janus-like NPs, providing strong interaction between PtFe and Fe_2C, contributes to their long-term ORR catalytic stability.

The alkaline ORR activities of the Janus-like PtFe-Fe_2C, PtFe NPs, Fe_2C NPs and commercial catalysts were also investigated. **Supplementary Fig. 9a** shows the ORR polarization curves obtained on a glassy carbon rotating disk electrode in O_2-saturated 0.1 M KOH solution at room temperature and a sweep rate of 10 mV s^{-1}. We further normalized the kinetic current calculated from the ORR polarization curve to Pt mass (**Supplementary Fig. 9b**), respectively. The mass activity at 0.9 V *vs* RHE, xxx times higher than that of PtFe NPs (0.09 A/mg_{Pt}) (**Fig. 2d**). The PtFe-Fe_2C Janus-like NPs exhibit the highest mass activities, 3.3 times those of commercial Pd/C (0.07 A/mg), and 2.1 times those of the commercial Pt/C (0.11 A/mg), respectively.

The ORR durability of the catalysts was evaluated by applying the cyclic potential sweeps at a sweep rate of 100 mV s^{-1} for 5 000 potential cycles. The PtFe-Fe_2C Janus-like NPs exhibit almost no ORR polarization curve shift after 5,000 potential cycles (**Supplementary Fig. 9c**). As a sharp contrast, the ORR polarization curves of the commercial Pd/C and the Pt/C show 16 and 10 mV negative shifts after durability tests, respectively (**Supplementary Fig. 9d**), showing that the PtFe-Fe_2C Janus-like NPs perform the best durability. Furthermore, ICP-AES shows only small Fe loss after the durability tests.

Theoretical investigation. DFT calculations were carried out to elucidate the origin of the enhanced ORR performance of interface catalysts at the microscopic level, The band structure shows this alloy has an anisotropic conducting behavior (**Supplementary Fig. 10a**). Especially to the paths along Z→R and X→Γ, they are both parallel the Fe→Fe directions in the real space. Therefore, the electronic transfer within the *fcc*-FePt goes through Fe-Pt-Fe instead of Fe-Fe. The partial density of states (PDOS) show the Pt-5d electrons occupy the levels higher than the Fe-3d orbitals (**Supplementary Fig. 10b**), while the lowest conducting states next to the Fermi level (E_F) are contributed by the Fe-3d anti-bonding orbitals. This indicates that the Pt sites shows more electronic activity than the Fe sites in the bulk phase of *fcc*-FePt. The bulk Fe_2C structure model was built within orthorhombic lattice (*PNNM)*. It shows a ferromagnetic spin-configuration (**Supplementary**

Fig. 10c) and the C-2p orbitals are staying between the Fe-3d bonding and anti-bonding orbitals occupying across the E_F. This system is also an anisotropic conducting behavior for electrons near the E_F., there are energetic barriers existing for electronic transitions along the paths of the T→Y and X→U parallel to the directions of C→C and Fe→Fe. Thus, the electronic transfer goes *via* the Fe→C→Fe. The PDOS illustrates both Fe-3d in spin-down and C-2p in spin-up orbital levels contributing to the electronic states near the E_F (Supplementary Fig. 10d). This system also has a good metallic behavior since the coupled *p-d* orbitals are transition allowed.

We further built the interface (IF) model (**Supplementary Fig. 8e**) to simulate the Janus-like NPs. The bonding and anti-bonding orbitals distributions show the interface region *(i.e.* FePt bonding with Fe_2C) tends to be more electron-rich while the charge densities are rather directionally distributed (**Supplementary Fig. 10e**). The PDOS gives more detail of the electronic properties differing from the interface and bulk regions by C-2p, Fe-3d, and Pt-5d electrons, respectively (**Supplementary Fig. 10f**). The C-2p electrons at the IF show higher activities than the ones in the bulk. 3d electrons of Fe at the IF dominate the levels nearby E_F, while the bulk Fe-3d electrons tends to have obvious e_g-to-t_{2g} splitting of the crystal-field effect in the bulk. The Pt-5d bonding electrons are pushed downward to lower levels with the broadened peak in absence of Van-Hove singularities. However, the Pt-5d electrons in the bulk region are pushed towards to the E_F. Thus, the electronic activities of Pt-5d orbitals are suppressed by the interface bonding between Fe_2C and FePt. Meanwhile, combining the interface carbonization with electron-rich FePt particles also enhance the electronic activities near the E_F.

The electronc structure calculation supports that, with Janus-like interface structural engineering, the active d orbitals of Fe and Pt sites have been obviously modified. The charge transfer between Fe→Pt→Fe and Fe→C→Fe turns to be stronger rather than the merely Fe→Fe. Moreover, the Fe-3d orbitals shows higher activity and strengthens the chemisorption of O_2 assisted by active C-2p via

interfacial Fe-C-Fe bonding. Meanwhile, the Pt-5d center downshifts toward lower level to prevent potentially over-binding the adsorbing intermediates (**Supplementary Materials, Fig. 11 a-f**).

The energy profile demonstrates catalytic ORR activities within acid condition (**Fig. 3a**) based on the proposed four-electron process. As we know, in general, the first step (O_2 to O_2*) determines the following activity of the electronic transfer from the catalyst support to the adsorbed intermediates. The final step reflects the energetic favorability of this ORR on the catalyst surface. While the energy barriers induced by the transition steps are mainly determined by the local morphology and bonding between the surface structure and absorbates. The overall ORR activities have been compared among the systems of Fe_2C||FePt, Fe_2C and FePt, respectively (**Fig. 3a**). Both Fe_2C||FePt and FePt have shown similar energy gain at the first step (O_2*+4H^++4e^-), which is the rate-determining step of the ORR process. They are -4.70 eV and -5.01 eV for Fe_2C||FePt and FePt respectively, while the energy-gain shows -4.02 eV for Fe_2C showing slightly less activity. This result consistently confirms the FePt is also rather active in ORR especially at the initiation step.

Regarding the energetic barriers from the simulated ORR process, we find both Fe_2C and FePt have barriers among the steps of transformation for species. The highest barrier for FePt is 2.14 eV while that for Fe_2C is 3.06 eV, meaning ORR is most difficulton the bare Fe_2C surface only. The high barrier for FePt is found to occur at the step from transforming the O_2*+4(H^++e^-) into *OOH+3(H^++e^-). For the Fe_2C, the barrier forms at transforming the *OH+H_2O+(H^++e^-) to the final product ($2H_2O$). This is actually an uphill process and potentially an energetic unfavorable for ORR on Fe_2C only. However, we find the interface system (Fe_2C||FePt) does not show any energetic barrier for the whole steps of the ORR process from O_2+4(H^++e^-) to $2H_2O$. The largest energetic gain

(-6.11 eV) is at the step of transforming the *O+H_2O+($2H^+$+e^-) to *OH+H_2O+(H^++e-), denoting the monoatomic O at the interface region is rather active to capture the near-itinerant (H^++e^-).

As for the energetic preference for the formation of the final product ($2H_2O$), the ΔG gives the largest gain with -16.36 eV for Fe_2C||FePt interface, while -6.45 eV and -1.47 eV for FePt and Fe_2C respectively. This further indicates that the ORR activity for Fe_2C is intrinsically not as high as FePt, especially to the final energetic contrast for the capability of forming the H_2O. Nevertheless, the limited activity of FePt compared to the Fe_2C||FePt may arise because the FePt system has energetic barriers among intermediate steps while the Fe_2C||FePt is barrier-free. The activity of the adsorbed O_2* to capture H^++e^- is stronger in the Fe_2C||FePt with an interface lattice rearrangement for minimization of whole surface energy. The Coulomb repulsive potential for electronic on-site transfer between H and O can be overcome or even compensated by such relaxations of local interfacial electron-lattice couplings. Thus, the interface (Fe_2C||FePt) wins and shows a downhill process, as an evident energy preferred of H_2O generation with a gained -16.36 eV.

Combined with **Fig. 3a** and **Fig. 3b**, we see that the catalytic ORR (acid-condition) at the Fe_2C||FePt shows an energetic barrier-free route map. This arises because the interfacial lattice relaxations reduce the barriers heights between different on-sites electron transfer, and also lower the Coulomb repulsive potentials of electron-electron coupling between different on-site orbitals. The IF induced empty states appearing on the Fe_2C surface enhance the feasibilities of the docking for the lone-pair electrons of the H_2O. The reason of evident lattice relaxation of the IF system arises from the largely unstable surface energy. Evident surface effect leads to a spontaneous minimization for surface energy following with charge distributions results in a continuous local lattice re-arrangement. Therefore, the IF (Fe_2C||FePt) not only produces a rich electronegativity area for promoting the charge transfer of ORR, but also reducing or annihilating the energetic barriers of each

intermediating steps whatever the appearance of the *OOH, *OH, or O*. Moreover, the local lattice relaxation for FePt region promotes the bonding cleavage of adsorbed O-O for enhancing the reaction activity of ORR steps.

Actually, we have also conducted an investigation on the energy profile within alkaline condition. The energy barrier free route-map for the Janus-like interface NP is maintained within similar physical trend, but less energetic gain than acid condition. This denotes the Pt activity not only well preserve but its d-band center is also modified to a lower level for higher turnover rate of intermediate steps. Meanwhile, the surface free energy minimization in Janus-like interface is a generalized mechanism for barrier-free ORR process independent to ambient solvent condition (**Supplementary Materials, Fig. 11a, b**).

We further move on to the energy profile to investigate catalytic ORR activities in alkaline medium, in terms of the change of free energy based on the proposed four-electron process. The overall ORR activities have been compared among the systems of Fe_2C||FePt, Fe_2C, and FePt, respectively (**Supplementary Fig. 11a**). Both Fe_2C||FePt and FePt have shown similar energy gain at the first step (O_2^{2-}*+2H_2O*), which is the rate-determining step of the ORR process. They are -3.29 eV and -3.37 eV for Fe_2C||FePt and FePt respectively. This result consistently confirms the FePt is also rather active in ORR especially at the initiation step. The FePt meets similar energy barrier of 1.59 eV compared to Fe_2C (1.15 eV) when these two systems proceed the catalytic step of forming OOH^-*+OH^-+H_2O. The final step of the formation of 4OH^- among these three catalyst systems shows differentiation into two different levels. For the Fe_2C and FePt sole catalyst support, the free energy levels of 4OH^- are mainly staying at -4.05 eV and -4.58 eV for Fe_2C while -4.36 eV for FePt, respectively. The ORR activity for Fe_2C is intrinsically not as high as FePt, since the first step (*i.e.* rate-determining step) shows the energetic contrast for the capability of charge transfer from the catalyst to the adsorbed O_2*. However, the limited activity of FePt may arise because the last transition toward 4OH^- is uphill process for FePt, while an always downhill process for Fe_2C||FePt

due to the interface lattice rearrangement for minimization of whole surface energy. Therefore, the Fe_2C||FePt, an evident energy preferred of $4OH^-$ generation system, wins because of gained -8.25 eV.

In detail, the Fe_2C interfaced with FePt and sole Fe_2C surface have been compared. The first primary advantage of the Fe_2C||FePt IF system is shown at the first step denoting the energetic preferred formation of the O_2* to O_2^{2-}* with an energy gain of -3.29 eV. As we can see, the Fe_2C without IF possesses an energy barrier of 1.15 eV from the step of O_2^{2-}* to transform into intermediate of OOH^-* in the presence of H_2O, while the Fe_2C||FePt IF system gives further energy downhill (-1.17 eV). This reaction step is actually also a determining step that guiding towards deep ORR level. The final steps show the Fe_2C||FePt catalytic ORR reaction gains an overall energy of -8.25 eV as the lowest level compared to the cases of Fe_2C without FePt interface (-4.05 eV or -4.58 eV). Combined with **Supplementary Fig. 11a** and **Supplementary Fig. 11b**, we see that the catalytic ORR Fe_2C||FePt shows an energetic barrier free route-map.

HER performance. The barrier-free interface electron transfer properties of the PtFe-Fe_2C Janus-like NPs motivated us to study their catalysis for other important electrochemical reactions. Here, we chose to study HER, an important half-reaction in the electrochemical water splitting for hydrogen generation. **Fig. 4a** shows the LSV curves of the commercial Pt/C, PtFe, Fe_2C and PtFe-Fe_2C Janus-like NPs in 0.5 M H_2SO_4. The results show that the activity increases in the order of Fe_2C < Pt/C < PtFe < PtFe-Fe_2C. To quantitatively compare the activities of these catalysts, the current densities at -0.07 V *vs* RHE in 0.5 M H_2SO_4 are summarized in **Fig. 4b**. The current density of Pt-based catalysts is much higher than that of the Fe_2C NPs, while the current density of PtFe-Fe_2C Janus-like NPs at -0.07 V in 0.5 M H_2SO_4 is 28.2 mA/cm^2, 1.7 times and 2.9 times higher than thaose of PtFe NPs (16.8 mA/cm^2) and the Pt/C (9.6 mA/cm^2), respectively. HER kinetics was also estimated by the corresponding Tafel plots (**Fig. 4c**). The Tafel slope for PtFe-Fe_2C Janus-like NPs is 23 mV/dec, lower than those of Pt/C (32 mV/dec) and PtFe (27 mV/dec), implying a faster HER rate on PtFe-Fe_2C Janus-like NPs. The catalyst durability was also assessed by applying 10,000

potential sweeps between -0.2 and 1.0 V (**Fig. 4d** and **Supplementary Fig. 12**). For the PtFe-Fe_2C Janus-like NPs show only 4 mV polarization curve shift at 10 mA/cm^2, lower than that of the commercial Pt/C (~8 mV) under the same condition. TEM analysis further confirms there is no morphology change of PtFe-Fe_2C Janus-like NPs after the HER stability test (**Supplementary Fig. 13 and 14**). These results prove that the PtFe-Fe_2C Janus-like NPs are a class of highly efficient interface catalyst for HER.

High H_2O_2 electrocatalytic performance and its high-sensitivity detection. With unique structural features, the PtFe-Fe_2C catalysts were further evaluated as enhanced electrocatalysts for high-sensitivity H_2O_2 detection. **Fig. 4e** shows the typical CVs of PtFe, Fe_2C and PtFe-Fe_2C Janus-like NPs for H_2O_2 reduction in N_2-saturated 0.1 M phosphate buffered saline (PBS, pH = 7.4) containing 4 mM H_2O_2. The PtFe-Fe_2C catalysts showed much higher activity for H_2O_2 than other control catalysts by judging from the measured current. The H_2O_2 detection sensitivity of the PtFe-Fe_2C Janus-like NPs was examined by a current−time (i−t) technique at a constant potential. **Fig. 4f** shows the typical amperometric responses of the PtFe-Fe_2C Janus-like NPs modified glassy carbon electrode upon the addition of H_2O_2 into the stirring 0.1 M PBS (pH 7.4) at −0.6 V *vs* Ag/AgCl. As H_2O_2 was added, the modified electrode responded rapidly to the substrate, achieving the maximum steady-state current within 2 s. Based on a signal-to-noise ratio (S/N) of 3, a very low detection limit of 2 nM can be obtained from these PtFe-Fe_2C Janus-like NPs. These result further reveal that PtFe-Fe_2C Janus-like NPs are a class of highly efficient interface catalyst for H_2O_2 high-sensitivity detection.

CONCLUSIONS

To summarize, we report the synthesis of a new class of Janus-like PtFe-Fe_2C NPs. The prepared interface catalyst displayed enhanced catalytic activity for the oxygen reduction**,** hydrogen evolution reactions and electrochemical detection of H_2O_2 than either PtFe or Fe_2C NPs. These NPs are also stable in the electrochemical conditions. DFT simulations reveal that the interface of Janus-like PtFe-Fe_2C NPs not only produce a rich electronegativity area for promoting the charge transfer of ORR, but also reducing or annihilating the energetic barriers of each intermediating steps. Moreover, the local lattice relaxation for FePt region promotes the bonding cleavage of adsorbed O-O for enhancing the reaction activity of ORR steps. The combination of PtFe and Fe_2C thus not only offers a solution to a critical problem of cathode ORR that has prevented practical application of polymer electrolyte membrane fuel cells but also pave the way for future development of efficient catalyst systems for more practical reactions.

METHODS

Preparation of PtFe-Fe_3O_4 Janus-like NPs. 100 mg of platinum(II) acetylacetonate ($Pt(acac)_2$), 0.19 mL of $Fe(CO)_5$, 1 mL of oleylamine, 1 mL of oleic acid and 10 mL of 1-octadecene were mixed and stirred. The crude reaction mixture containing the FePt NPs that had formed upon heating at 180 °C for 1 hwas further heated to 300 °C (under N_2) at a rate of approximately 8 °C/min and kept at this temperature for an additional 1 h. Under these circumstances, thermal decomposition of excess iron oleate complexes in the solution led to the generation of iron oxide. The black colloidal products were collected by centrifugation and washed two or three times with an ethanol/cyclohexane mixture before it was naturally cooled to temperature.

Preparation of PtFe-Fe_2C Janus-like NPs. In a four-neck flask, a mixture of 10 mg of PtFe-Fe_3O_4 dumbbell-like NPs, 3.1 mg of octadecylamine and 5 mL of oleylamine was stirred

sufficiently and degassed under a flow of Ar for 30 min at 120 ºC. The mixture was further heated to 320 ºC at 8 °C/min and kept for 5 h. The black colloidal products were collected by centrifugation and washed two or three times with an ethanol/cyclohexane mixture before it was naturally cooled to temperature.

Preparation of PtFe NPs. The PtFe NPs were synthesized as reported with a modification.[37] 39.4 mg of $Pt(acac)_2$ and 20 mL of OAm were first mixed with 35.4 mg $Fe(acac)_3$ at room temperature, respectively. Then the solution was further heated to 300 °C at a heating rate of 5 °C/min and kept at 300 °C for 1 h. Then the NPs were separated and purified by using hexane, ethanol, and centrifugation. Finally, the particles were kept in hexane.

Preparation of Fe_2C NPs. The Fe_2C NPs were synthesized as reported with a modification.[34] 20 mL of 1-octadecene, 9.8 mg of NH_4Br and 0.32 mL of oleylamine were mixed magnetically and degassed under a gentle N_2 flow for 30 min in a four-neck flask. The solution was then heated to 120 °C and kept at this temperature for 30 min before it was heated further to 180 °C to fully remove the organic impurities. After that, 0.13 mL $Fe(CO)_5$ was injected to the reaction mixture and kept there for 30 min. A color change from salmon to brown then to black of the solvents were observed after ca. 1 min, indicating the decomposition of $Fe(CO)_5$ and the formation of *bcc*-Fe NPs. To control the oxidation of the as-prepared *bcc*-Fe NPs, 0.32 mL of oleic acid and 0.2 mL of hexane were added, and the resultant solution was aged at 140 °C for another 30 min before it was cooled down to room temperature. Then, the NPs were also separated and purified by using centrifugation. Finally, the particles were kept in hexane. A mixture of 3.1 mg of octadecylamine and 5 mL of oleylamine was magnetically blended in a four-neck flask and degassed under a gentle N_2 flow for 30 min at 120 ºC. Then, the as-prepared *bcc*-Fe NPs (in 10 mL hexane) were added, and the reaction solution was heated at 130 ºC for another 30 min to

remove hexane thoroughly before it was heated to 260 ºC for 30 min. The black colloidal products were collected by centrifugation and washed two or three times with an ethanol/cyclohexane mixture before it was naturally cooled to temperature.

Characterization. The morphologies of the samples were characterized by transmission electron microcopy (TEM) and high resolution TEM (HRTEM) on a FEI Tecnai-G2 F30 at an accelerating voltage of 300 KV. Powder X-ray diffraction (XRD) spectra were recorded on a X'Pert-Pro MPD diffractometer (Netherlands PANalytical) operating at 40 KV and 40 mA with Cu Kα radiation. The concentrations of catalysts were determined by the inductively coupled plasma atomic emission spectrometer (Varian 710-ES). X-ray photoelectron spectra (XPS) were collected with an SSI S-Probe XPS Spectrometer. The catalysts after the durability tests were scratched off the glassy carbon electrode with the aid of sonication in ethanol, and then collected for further TEM characterization.

Electrochemical measurements. Electrochemical measurements were conducted on a CHI760 Electrochemical Workstation (Shanghai Chenhua Instrument Corporation, China) in a conventional three-electrode cell by using a platinum plate (for ORR) or graphite rod electrode (for HER) as the counter electrode and a saturated calomel electrode as the reference electrode. The working electrode was a glassy carbon Rotating Disk Electrode (RDE, diameter: 5 mm, area: 0.196 cm^2). The different catalysts were dispersed in isopropanol + ultrapure water + 5% Nafion (*v:v:v* 3:1:0.004) to reach a homogeneous catalyst ink with a concentration of 1 mg/mL by sonicating for 1 h. Then, 10 μL of the catalyst was dropped onto the surface of the RDE for further electrochemical tests. The ORR measurements were performed in oxygen-saturated 0.1 M $HClO_4$ solution using RDE, and the accelerated durability tests (ADTs) were performed in 0.1 M $HClO_4$ solution by applying the cyclic potential sweeps between 0.6 V-1.1 V *vs* saturated

calomel electrode for 5,000 cycles. The ORR measurements were further performed in oxygen-saturated 0.1 M KOH solution using RDE, and the accelerated durability tests (ADTs) were performed in 0.1 M KOH solution by applying the cyclic potential sweeps between 0.4 V-1.0 V *vs* RHE for 5000 cycles. The HER measurements were performed in N_2-saturated 0.5 M H_2SO_4 solution using RDE, and the accelerated durability tests (ADTs) were performed in 0.5 M H_2SO_4 solution by applying the cyclic potential sweeps between -0.2 V-1.0 V *vs* saturated calomel electrode for 10,000 cycles. The H_2O_2 detection were performed in 0.1 M phosphate buffer solution (PBS, pH 7.4).

DFT calculations.

ACKNOWLEDGMENTS

This work was financially supported by the National Natural Science Foundation of China (51671003), National Basic Research Program of China (No. 2017YFA0206701 and No. 2016YFB0100201), Open Project Foundation of State Key Laboratory of Chemical Resource Engineering, the start-up supports from Peking University and Young Thousand Talented Program.

Author contributions

J.L. and S.G. designed and conducted the experiments, performed the analysis and wrote the manuscript, B.H. performed the DFT simulations and all authors discussed the results and commented on the manuscript.

REFERENCES

1. Debe, M. K. Electrocatalyst approaches and challenges for automotive fuel cells.*Nature* **486**, 43-51 *(*2012).

2. Shao, M., Chang, Q., Dodelet, J.-P., Chenitz, R. Recent Advances in Electrocatalysts for Oxygen Reduction Reaction.*Chem. Rev.* **116**, 3594-3657 *(*2016).

3. Gasteiger, H. A., Marković, N. M. Just a Dream—or Future Reality?*Science* **324**, 48-49 *(*2009).

4. Gasteiger, H. A., Kocha, S. S., Sompalli, B., Wagner, F. T. Activity benchmarks and requirements for Pt, Pt-alloy, and non-Pt oxygen reduction catalysts for PEMFCs.*Appl. Catal. B: Environ.* **56**, 9-35 *(*2005).

5. Stephens, I. E. L., Bondarenko, A. S., Gronbjerg, U., Rossmeisl, J., Chorkendorff, I. Understanding the electrocatalysis of oxygen reduction on platinum and its alloys.*Energy Environ. Sci.* **5**, 6744-6762 *(*2012).

6. Wang, Y.-J., Zhao, N., Fang, B., Li, H., Bi, X. T., Wang, H. Carbon-Supported Pt-Based Alloy Electrocatalysts for the Oxygen Reduction Reaction in Polymer Electrolyte Membrane Fuel Cells: Particle Size, Shape, and Composition Manipulation and Their Impact to Activity.*Chem. Rev.* **115**, 3433-3467 *(*2015).

7. Wang, W., Lei, B., Guo, S. Engineering Multimetallic Nanocrystals for Highly Efficient Oxygen Reduction Catalysts.*Adv. Energy Mater.* **6**, DOI: 10.1002/aenm.201600236 *(*2016).

8. Guo, S., Zhang, S., Sun, S. Tuning Nanoparticle Catalysis for the Oxygen Reduction Reaction.*Angew. Chem. Int. Ed.* **52**, 8526-8544 *(*2013).

9. Lv, H., Li, D., Strmcnik, D., Paulikas, A. P., Markovic, N. M., Stamenkovic, V. R. Recent Advances in the Design of Tailored Nanomaterials for Efficient Oxygen Reduction Reaction.*Nano Energy* **29**, 149-165 *(*2016).

10. Adzic, R. R., Zhang, J., Sasaki, K., Vukmirovic, M. B., Shao, M., Wang, J. X., Nilekar, A. U., Mavrikakis, M., Valerio, J. A., Uribe, F. Platinum Monolayer Fuel Cell Electrocatalysts.*Top. Catal.* **46**, 249-262 *(*2007).

11. Zhang, J., Sasaki, K., Sutter, E., Adzic, R. R. Stabilization of Platinum Oxygen-Reduction Electrocatalysts Using Gold Clusters.*Science* **315**, 220-222 *(*2007).

12. Stamenkovic, V. R., Fowler, B., Mun, B. S., Wang, G., Ross, P. N., Lucas, C. A., Marković, N. M. Improved Oxygen Reduction Activity on Pt3Ni(111) via Increased Surface Site Availability.*Science* **315**, 493-497 *(*2007).

13. Stamenkovic, V. R., Mun, B. S., Arenz, M., Mayrhofer, K. J. J., Lucas, C. A., Wang, G., Ross, P. N., Markovic, N. M. Trends in electrocatalysis on extended and nanoscale Pt-bimetallic alloy surfaces.*Nat. Mater.* **6**, 241-247 *(*2007).

14. Lim, B., Jiang, M., Camargo, P. H. C., Cho, E. C., Tao, J., Lu, X., Zhu, Y., Xia, Y. Pd-Pt Bimetallic Nanodendrites with High Activity for Oxygen Reduction. *Science* **324**, 1302-1305 *(*2009).

15. Snyder, J., Fujita, T., Chen, M. W., Erlebacher, J. Oxygen reduction in nanoporous metal–ionic liquid composite electrocatalysts.*Nat. Mater.* **9**, 904-907 *(*2010).

16. Strasser, P., Koh, S., Anniyev, T., Greeley, J., More, K., Yu, C., Liu, Z., Kaya, S., Nordlund, D., Ogasawara, H., Toney, M. F., Nilsson, A. Lattice-strain control of the activity in dealloyed core–shell fuel cell catalysts.*Nat. Chem.* **2**, 454-460 *(*2010).

17. Strmcnik, D., Escudero-Escribano, M., Kodama, K., StamenkovicVojislav, R., Cuesta, A., Marković, N. M. Enhanced electrocatalysis of the oxygen reduction reaction based on patterning of platinum surfaces with cyanide.*Nat. Chem.* **2**, 880-885 *(*2010).

18. van der Vliet, D. F., Wang, C., Tripkovic, D., Strmcnik, D., Zhang, X. F., Debe, M. K., Atanasoski, R. T., Markovic, N. M., Stamenkovic, V. R. Mesostructured thin films as electrocatalysts with tunable composition and surface morphology.*Nat. Mater.* **11**, 1051-1058 *(*2012).

19. Cui, C., Gan, L., Heggen, M., Rudi, S., Strasser, P. Compositional segregation in shaped Pt alloy nanoparticles and their structural behaviour during electrocatalysis.*Nat. Mater.* **12**, 765-771 *(*2013).

20. Wang, D., Xin, H. L., Hovden, R., Wang, H., Yu, Y., Muller, D. A., DiSalvo, F. J., Abruña, H. D. Structurally ordered intermetallic platinum–cobalt core–shell nanoparticles with enhanced activity and stability as oxygen reduction electrocatalysts.*Nat. Mater.* **12**, 81-87 *(*2013).

21. Chen, C., Kang, Y., Huo, Z., Zhu, Z., Huang, W., Xin, H. L., Snyder, J. D., Li, D., Herron, J. A., Mavrikakis, M., Chi, M., More, K. L., Li, Y., Markovic, N. M., Somorjai, G. A., Yang, P., Stamenkovic, V. R. Highly Crystalline Multimetallic Nanoframes with Three-Dimensional Electrocatalytic Surfaces.*Science* **343**, 1339-1343 *(*2014).

22. Hernandez-Fernandez, P., Masini, F., McCarthy, D. N., Strebel, C. E., Friebel, D., Deiana, D., Malacrida, P., Nierhoff, A., Bodin, A., Wise, A. M., Nielsen, J. H., Hansen, T. W., Nilsson, A., StephensIfan, E. L., Chorkendorff, I. Mass-selected nanoparticles of PtxY as model catalysts for oxygen electroreduction.*Nat. Chem.* **6**, 732-738 *(*2014).

23. Calle-Vallejo, F., Tymoczko, J., Colic, V., Vu, Q. H., Pohl, M. D., Morgenstern, K., Loffreda, D., Sautet, P., Schuhmann, W., Bandarenka, A. S. Finding optimal surface sites on heterogeneous catalysts by counting nearest neighbors.*Science* **350**, 185-189 *(*2015).

24. Huang, X., Zhao, Z., Cao, L., Chen, Y., Zhu, E., Lin, Z., Li, M., Yan, A., Zettl, A., Wang, Y. M., Duan, X., Mueller, T., Huang, Y. High-performance transition metal–doped Pt3Ni octahedra for oxygen reduction reaction.*Science* **348**, 1230-1234 *(*2015).

25. Zhang, L., Roling, L. T., Wang, X., Vara, M., Chi, M., Liu, J., Choi, S.-I., Park, J., Herron, J. A., Xie, Z., Mavrikakis, M., Xia, Y. Platinum-based nanocages with subnanometer-thick walls and well-defined, controllable facets.*Science* **349**, 412-416 *(*2015).

26. Bu, L., Zhang, N., Guo, S., Zhang, X., Li, J., Yao, J., Wu, T., Lu, G., Ma, J.-Y., Su, D., Huang, X. Biaxially strained PtPb/Pt core/shell nanoplate boosts oxygen reduction catalysis.*Science* **354**, 1410-1414 *(*2016).

27. Escudero-Escribano, M., Malacrida, P., Hansen, M. H., Vej-Hansen, U. G., Velázquez-Palenzuela, A., Tripkovic, V., Schiøtz, J., Rossmeisl, J., Stephens, I. E. L., Chorkendorff, I. Tuning the activity of Pt alloy electrocatalysts by means of the lanthanide contraction.*Science* **352**, 73-76 *(*2016).

28. He, D., Zhang, L., He, D., Zhou, G., Lin, Y., Deng, Z., Hong, X., Wu, Y., Chen, C., Li, Y. Amorphous nickel boride membrane on a platinum-nickel alloy surface for enhanced oxygen reduction reaction.*Nat. Commun.* **7**, 12362 *(*2016).

29. Ganesan, R., Lee, J. S. Tungsten Carbide Microspheres as a Noble-Metal-Economic Electrocatalyst for Methanol Oxidation.*Angew. Chem. Int. Ed.* **44**, 6557-6560 *(*2005).

30. Lukatskaya, M. R., Mashtalir, O., Ren, C. E., Dall'Agnese, Y., Rozier, P., Taberna, P. L., Naguib, M., Simon, P., Barsoum, M. W., Gogotsi, Y. Cation Intercalation and High Volumetric Capacitance of Two-Dimensional Titanium Carbide.*Science* **341**, 1502-1505 *(*2013).

31. Chen, W.-F., Muckerman, J. T., Fujita, E. Recent developments in transition metal carbides and nitrides as hydrogen evolution electrocatalysts. *Chem. Commun.* **49**, 8896-8909 *(*2013).

32. Figuerola, A., Fiore, A., Di Corato, R., Falqui, A., Giannini, C., Micotti, E., Lascialfari, A., Corti, M., Cingolani, R., Pellegrino, T., Cozzoli, P. D., Manna, L. One-Pot Synthesis and Characterization of Size-Controlled Bimagnetic FePt−Iron Oxide Heterodimer Nanocrystals.*J. Am. Chem. Soc.* **130**, 1477-1487 *(*2008).

33. Bonnet, F., Ropital, F., Lecour, P., Espinat, D., Huiban, Y., Gengembre, L., Berthier, Y., Marcus, P. Study of the oxide/carbide transition on iron surfaces during catalytic coke formation.*Surf. Interface Anal.* **34**, 418-422 *(*2002).

34. Yang, Z., Zhao, T., Huang, X., Chu, X., Tang, T., Ju, Y., Wang, Q., Hou, Y., Gao, S. Modulating the phases of iron carbide nanoparticles: from a perspective of interfering with the carbon penetration of Fe@Fe3O4 by selectively adsorbed halide ions.*Chem. Sci.* **8**, 473-481 *(*2017).

35. Yao, S., Yang, C., Zhao, H., Li, S., Lin, L., Wen, W., Liu, J., Hu, G., Li, W., Hou, Y., Ma, D. Reconstruction of the Wet Chemical Synthesis Process: The Case of Fe5C2 Nanoparticles.*J. Phys. Chem. C* **121**, 5154-5160 *(*2017).

36. Goto, Y., Taniguchi, K., Omata, T., Otsuka-Yao-Matsuo, S., Ohashi, N., Ueda, S., Yoshikawa, H., Yamashita, Y., Oohashi, H., Kobayashi, K. Formation of Ni3C Nanocrystals by Thermolysis of Nickel Acetylacetonate in Oleylamine: Characterization Using Hard X-ray Photoelectron Spectroscopy.*Chem. Mater.* **20**, 4156-4160 *(*2008).

37. Yu, Y., Yang, W., Sun, X., Zhu, W., Li, X. Z., Sellmyer, D. J., Sun, S. Monodisperse MPt (M = Fe, Co, Ni, Cu, Zn) Nanoparticles Prepared from a Facile Oleylamine Reduction of Metal Salts.*Nano Lett.* **14**, 2778-2782 *(*2014).

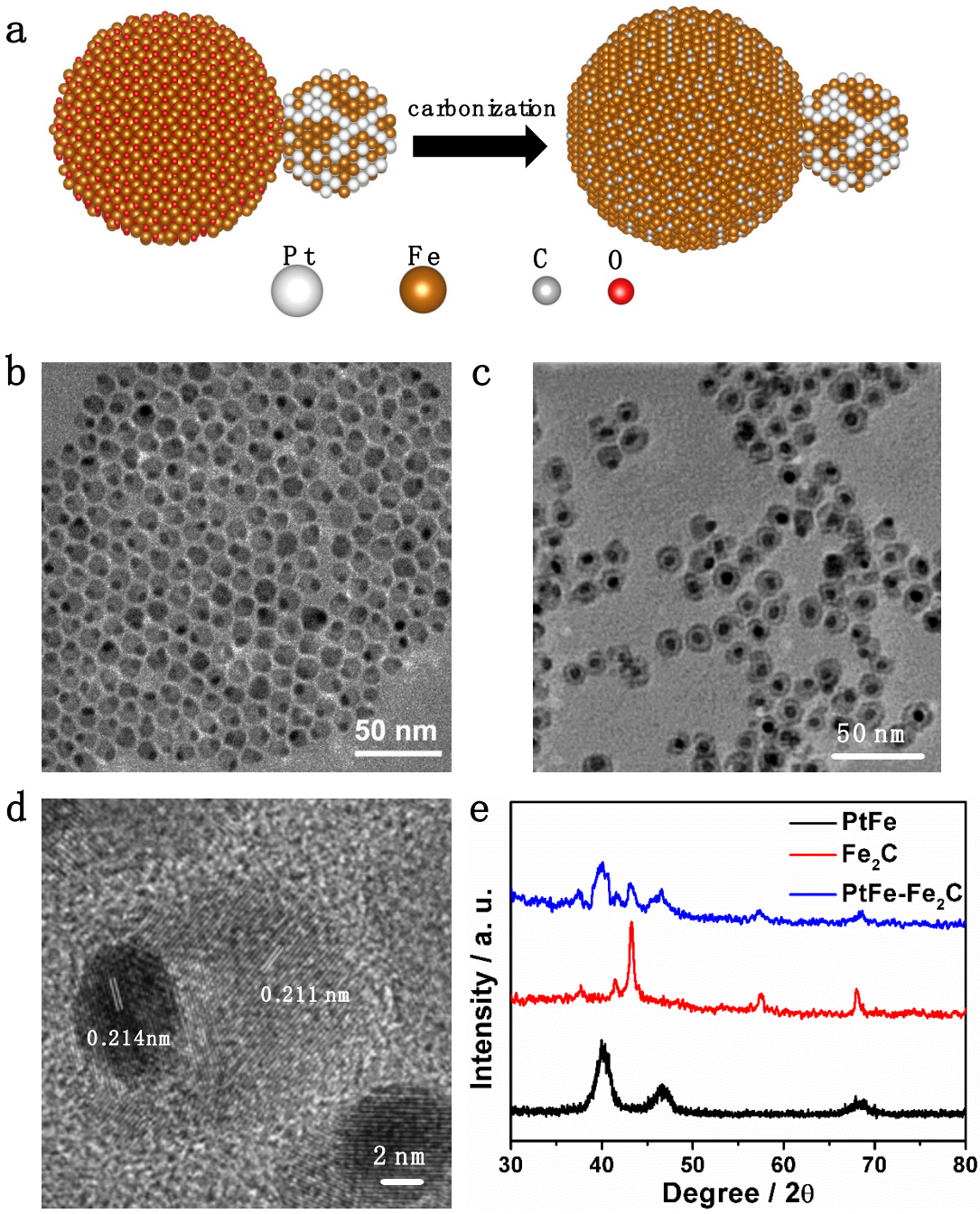

Figure 1. Synthetic strategy and physical characterization of PtFe–Fe_2C Janus-like NPs. (a) Schematic illustration of the formation process of PtFe-Fe_2C Janus-like NPs. TEM images of (b) PtFe-Fe_3O_4 Janus-like NPs and (c) PtFe-Fe_2C Janus-like NPs. (d) HRTEM images of PtFe–Fe_2C Janus-like NPs. (e) XRD patterns of PtFe NPs, Fe_2C NPs, and PtFe–Fe_2C Janus-like NPs.

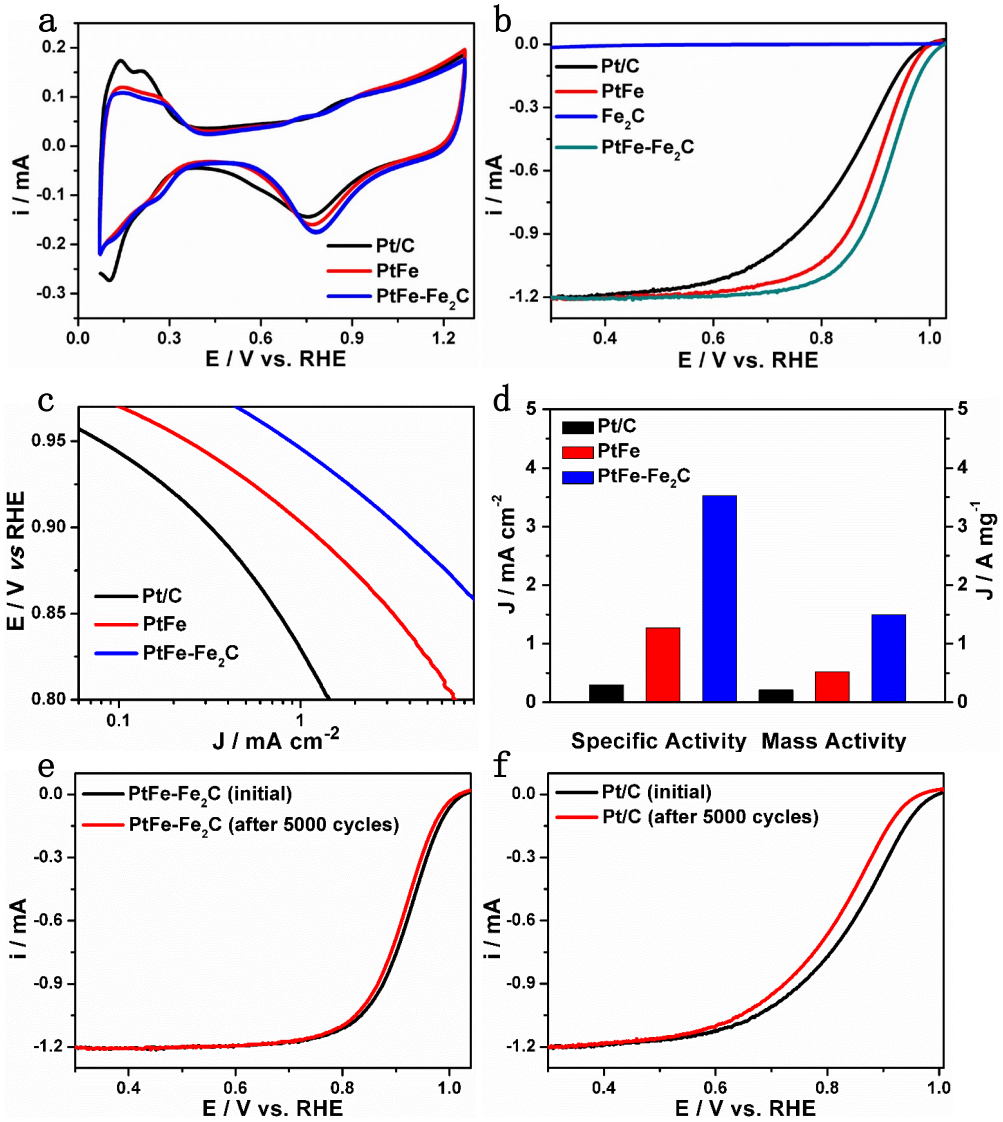

Figure 2. ORR performance of PtFe-Fe$_2$C, PtFe and Fe$_2$C NPs. (a) CVs of different electrocatalysts in 0.1 M $HClO_4$. (b) ORR polarization curves, (c) Tafel plots and (d) specific activities and mass activities of different catalysts at 0.9 V *vs.* RHE. The ORR polarization curves were recorded at room temperature in an O_2-saturated 0.1 M $HClO_4$ solution. (e) ORR polarization curves of the PtFe−Fe$_2$C Janus-like NPs catalyst before and after 5,000 cycles between 0.6-1.1 V *vs.* RHE. (f) ORR polarization curves of the commercial Pt/C catalyst before and after 5,000cycles between 0.6-1.1 V *vs.* RHE.

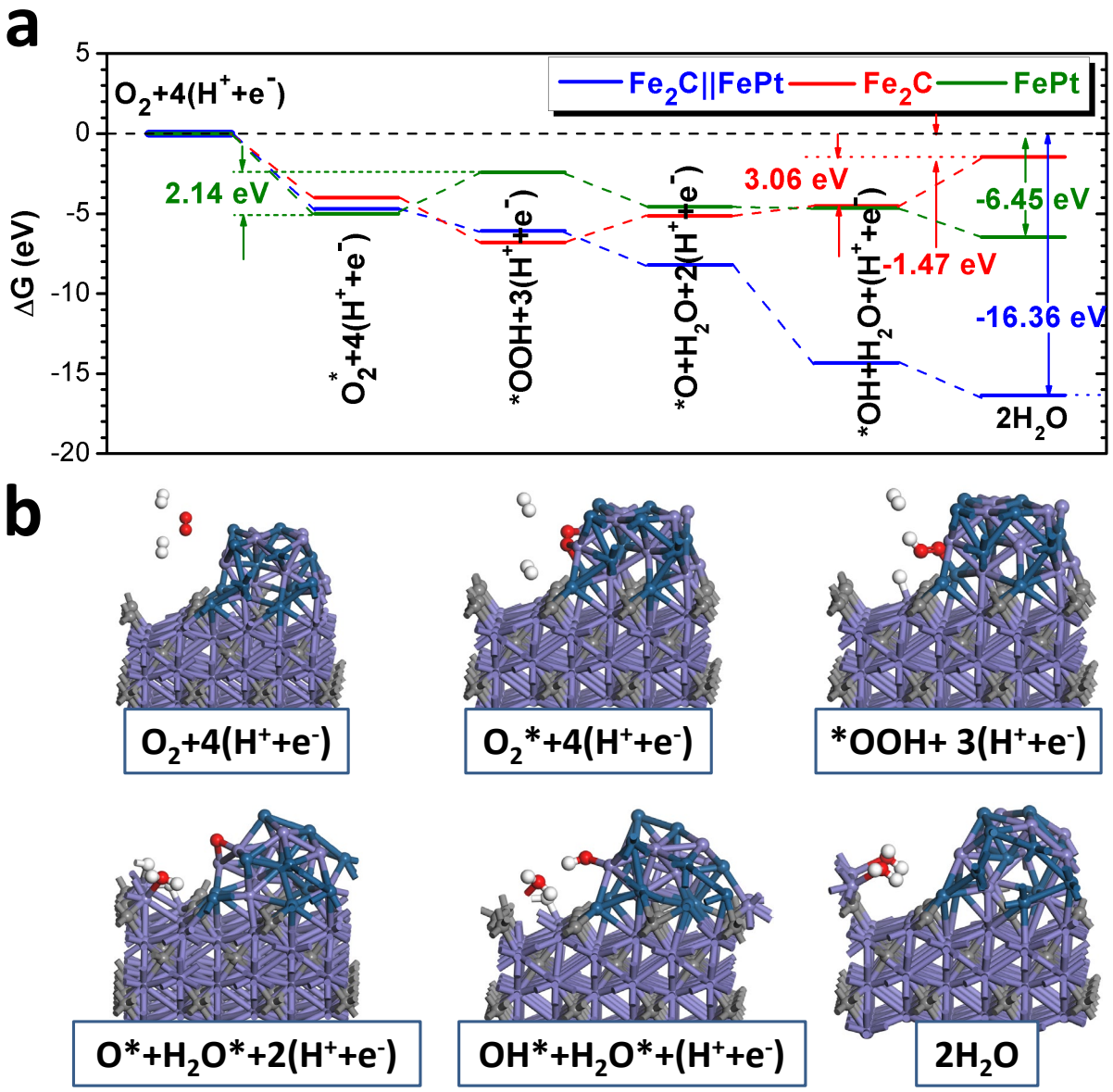

Figure 3. (a) The free energy-level diagram of the catalytic ORR (acid-condition) steps conducted on the Fe_2C||FePt IF system and Fe_2C without FePt-IF system. **(b)** The local structures and bonding variations of O_2*, H*, *OOH*, OH*, and H_2O* in the simulation for interpreting the catalytic ORR (acid-condition) mechanism on the Fe_2C||FePt IF system. (Pt=dark green, Fe=light purple, C=grey, O=red, and H=white).

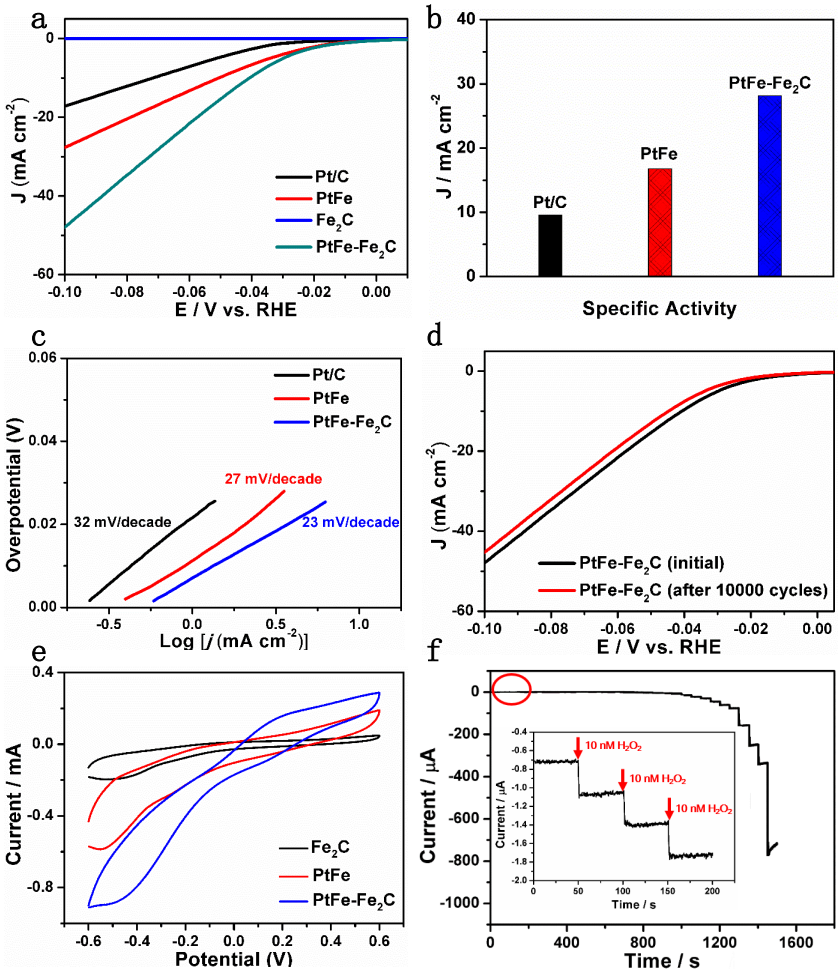

Figure 4. HER and H_2O_2 reduction electrocatatic performance of PtFe-Fe_2C, PtFe and Fe_2C NPs. (a) HER polarization curves of different electrocatalysts in 0.5 M H_2SO_4 with iR-compensation. (b) Specific activities of different catalysts at -0.07 V *vs* RHE. (c) The corresponding Tafel plots. (d) HER polarization curves of PtFe−Fe_2C Janus-like NPs before and after 10,000 CV cycles. (e) CVs of different electrocatalysts in N_2-saturated 0.1 M PBS (7.4) solution containing 4 mM H_2O_2 at a scan rate of 100 mV s^{-1}. (f) Amperometric responses of different electrocatalysts modified glassy carbon electrode to the successive addition of H_2O_2 in PBS at an applied potential of −0.6 V *vs* Ag/AgCl. The *inset* shows a close look of the red circle with the H_2O_2 concentration from 10 to 50 nM.